Tectonophysics 819 (2021) 229104

Contents lists available at ScienceDirect

Tectonophysics

journal homepage: www.elsevier.com/locate/tecto

Sedimentary and crustal velocity structure of Trans-North China Orogen from joint inversion of Rayleigh wave phase velocity and ellipticity and some implication for Syn-rift volcanism

Xiang Huang [a,b,c], Zhifeng Ding [a,*], Jieyuan Ning [b], Fenglin Niu [c], Guoliang Li [d], Xingchen Wang [a], Xiaoming Xu [a]

[a] Institute of Geophysics, China Earthquake Administration, Beijing 100081, China
[b] School of Earth and Space Sciences, Peking University, Beijing 100871, China
[c] Department of Earth, Environmental and Planetary Sciences, Rice University, Houston 77005, TX, USA
[d] Department of Earth and Environmental Sciences, Michigan State University, East Lansing 48824, MI, USA

ARTICLE INFO

Keywords:
Ambient noise tomography
Rayleigh wave ellipticity
Joint inversion
Sedimentary thickness
North China Craton
ChinArray

ABSTRACT

We present a high-resolution 3-D shear wave velocity model of the crust and uppermost mantle beneath the Trans-North China Orogen and its adjacent regions derived from a joint inversion of Rayleigh wave phase velocity and ellipticity computed from ambient noise data. The 3-D velocity model reveals large lateral variations in sedimentary and crustal structure across the study area. In addition to the large velocity contrast between the North China Basin and the Ordos Basin located in the east and west sides of the orogen, we found a northward thinning of sediments within the Weihe-Shanxi Rift System that sits in the middle of the orogen, suggesting that the rifting has likely propagated from the Weihe Rift in the south to the Shanxi Rift in the north during the Oligocene-Pliocene. While the north-south trending rift is underlaid by a low Vs across the entire range in the upper and middle crust, only the north segment, which houses the Datong volcanic complex, exhibits a substantial low velocity structure in the lower crust and the uppermost mantle. The center of the low velocity anomaly extends into the uppermost mantle at a location approximately 150 km west to the volcanic complex, which is speculated for a nearly horizontal channel in the lower crust for the upwelling of the hot materials from the asthenosphere. These observations suggest that Shanxi Rift in the north is a more active segment within the rift system, which is manifested by the Quaternary *syn*-rift Datong volcanic complex.

1. Introduction

Archean cratons are commonly characterized by a thick, cold, and depleted lithosphere with less iron and garnet, which makes them buoyant and stable on Earth's surface for billion years. However, the North China Craton (NCC), one of the oldest cratons on Earth, has experienced strong tectonic activation since the Mesozoic, leading to the replacement of the stable keel with a thin and fertile mantle lithosphere (Menzies et al., 1993; Griffin et al., 1998). In light of previous studies, the NCC consists of three parts: the western NCC, the eastern NCC, and the Trans-North China Orogen (TNCO) (Zhao et al., 2005) (Fig. 1). The western NCC, including mainly the Ordos Basin, has a relatively stable lithosphere which remains intact since the Precambrian. On the contrary, the North China Basin (NCB) in the eastern part experienced dramatic destruction in the Mesozoic and Cenozoic resulting from the subductions of Pacific Plate and the extrusion of the Tibetan Plateau (Bao et al., 2013; Ai et al., 2019). The TNCO is a nearly north-south-trending belt which is considered to have been formed by the collision of the western and eastern NCC, which is preceded by a subduction with a polarity yet to be determined. Geochemical and geological data suggested that the collision occurred at ~1.85 Ga ago, which resulted in the final amalgamation of the NCC (Zhao et al., 2005).

The TNCO is composed of the Taihang Mountains, Luliang Mountains, and the Weihe-Shanxi Rift System (WSRS) in-between (Fig. 1), which is one of the largest Cenozoic intracontinental rift systems (Bao et al., 2013). The WSRS comprises a series of rifted basins, extending

* Corresponding author at: Institute of Geophysics, China Earthquake Administration, No.5 South Road of Minzu University, Haidian District, Beijing 100081, China.
E-mail address: dingzf@cea-igp.ac.cn (Z. Ding).

https://doi.org/10.1016/j.tecto.2021.229104
Received 28 April 2021; Received in revised form 12 September 2021; Accepted 3 October 2021
Available online 8 October 2021

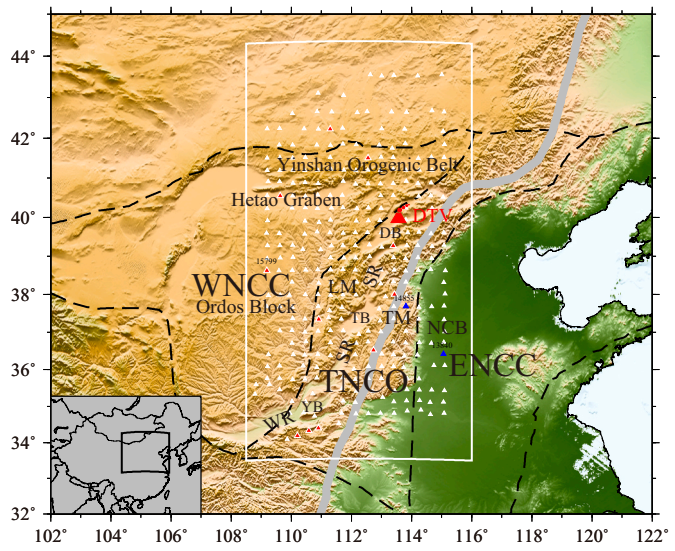

Fig. 1. Geological settings of the TNCO and its surrounding regions. Black dashed lines outline the main tectonic units: the western North China Craton (WNCC), the Trans-North China Orogen (TNCO), and the eastern North China Craton (ENCC), modified after Zhao et al. (2005). The big red triangle marks the location of Datong volcanic complex (DTV). The thick gray line represents the north-south gravity line. SR: Shanxi Rift; WR: Weihe Rift; NCB: North China Basin; LM: Luliang Mountains; TM: Taihang Mountains; DB: Datong Basin; TB: Taiyuan Basin; YB: Yuncheng Basin. The small triangles mark the 306 seismic stations used in this study. The two stations in blue are 14855 in Taihang Mountains and 13840 in NCB. The 11 small red triangles indicate the stations without robust Z/H ratio. The white rectangle outlines our study region. (For interpretation of the references to colour in this figure legend, the reader is referred to the web version of this article.)

from northern TNCO in the north via Taiyuan basin to the southeastern margin of Ordos Basin in the south. Magmatism mainly happened in the northern part of the WSRS, leading to the formation of Datong volcanic complex, which is one of the largest Quaternary intraplate volcanic complexes in NCC (Chen et al., 1992). According to previous studies, the surface topography, gravity anomalies and lithospheric thickness vary significantly across the TNCO (Zhu et al., 2011, 2012). The boundary between the eastern edge of the Taihang Mountains and the NCB is not only a topographic boundary, but also a boundary of gravity fields (Tang et al., 2011). As the boundary of western and eastern NCC, two completely different geological tectonic blocks, TNCO is an ideal place to study the connection between surface observations and subsurface seismic structures.

Seismic structure of the NCC and its adjacent regions has been extensively investigated with various seismic imaging techniques. For instance, receiver functions (Zheng et al., 2009; Chen et al., 2009; Wang et al., 2014a; Wang et al., 2016), body wave tomography (Tian et al., 2009; Xu and Zhao, 2009; Santosh et al., 2010; Zhao et al., 2012), ballistic surface wave tomography (Huang et al., 2009; An et al., 2009; Li et al., 2009; Jiang et al., 2013), ambient noise tomography (Fang et al., 2010; Zheng et al., 2011; Bao et al., 2013; Cheng et al., 2013) and many kinds of joint inversion methods (Tang et al., 2013; Bao et al., 2015; Guo and Chen, 2017; Li et al., 2018b; Ai et al., 2019) have been employed to study the structure of crust and upper mantle beneath this region. However, the 3-D sedimentary and upper crustal structures were generally less constrained due to limitations in seismic data used in previous studies.

The WSRS is one of the most important tectonic units of TNCO and has attracted the attention of a number of researchers. Geological studies of Cenozoic continental deposits suggest that during the Oligocene-Pliocene the rifting started from the Weihe Rift in the south and gradually extended to the Shanxi Rift in the north (Zhang et al., 1998). However, geological samples are limited in space, and a high-resolution 3-D model of sedimentary structure of the entire rift is preferred to understand its formation and evolution. In fact, the development mechanism of WSRS is still debated. The first point of view is that the extensive deformation of NCC might be associated with the westward subduction of the Pacific Plate in the east (Northrup et al., 1995; Yin and Harrison, 2000). Another theory believed that the far-field effects of the India-Eurasia collision could cause the intra-continental rift of NCC (Liu et al., 2004). There is also a conciliatory view that the extensive deformation of NCC is associated with both the northeastward escape of Tibetan Plateau and the subduction of the Pacific Plate (Xu et al., 2004; Zhang et al., 2003; Bao et al., 2013).

The Datong volcanic complex is located in the northern end of the WSRS. It began to erupt in the early Pleistocene and the volcanism continued to the late Pleistocene (Chen et al., 1992; Xu et al., 2005). Many seismic tomography studies have been carried out (Zhao et al., 2009; Lei, 2012; Tang et al., 2013; Guo et al., 2015; Li et al., 2018b) in order to investigate the origin of the intraplate volcanism, which is, however, still controversial. For instance, Huang and Zhao (2006) found a low velocity zone (LVZ) in the upper mantle under the volcanic complex and suggested that the volcanism originated from the dehydration of the stagnant Pacific Plate, whereas Zhao et al. (2009) and Lei (2012) found that the LVZ extend into the lower mantle and suggested the Datong volcanism is fed by a deep-rooted mantle plume. Besides, Li et al. (2018b) found a westward dipping LVZ, which was interpreted as an asthenosphere flow driven by the northeastward motion of the Tibetan Plateau.

For the past few years, ambient noise tomography has been widely applied to different regions all over the world (e.g., Shapiro, 2005; Yang et al., 2007; Yao et al., 2008; Zheng et al., 2008). The dominant period band of ambient noise lies between ~8 and 40 s (Zheng et al., 2011), the measured phase velocities in this period range are almost insensitive to crustal structures shallower than ~3 km (Lin et al., 2012). Meanwhile, velocity structure at shallow depth is very important for studying the relationship between surface tectonic settings and crustal structure, characterizing strong ground motion (Vidale and Helmberger, 1988), and constraining deeper structure more accurately (Waldhauser et al., 2002; Langston, 2011). Rayleigh wave ellipticity, or Z/H ratio, defined as the amplitude ratio between the vertical and radial components, has been proved to be particularly sensitive to shallow crustal structure (e.g., Boore and Nafi Toksöz, 1969).

Accurately measuring Rayleigh wave Z/H ratios is very challenging in the past due to low quality of horizontal records. Recent developments in 3-D broadband data and analysis techniques (Tanimoto and Alvizuri, 2006; Ferreira and Woodhouse, 2007) have made it possible to include the Z/H ratio measurements in constraining crustal structures (e.g., Yano et al., 2009; Lin et al., 2012; Lin and Schmandt, 2014; Chong et al., 2015). In this study, we jointly inverted the Rayleigh wave phase velocities at 6–40 s and Z/H ratios at 10–24 s derived from ambient noise cross-correlation functions of more than 300 broadband stations installed during the Phase III deployment of the ChinArray Project (ChinArray-Himalaya, 2011) to obtain a 3-D Vs model with high resolution beneath the TNCO and adjacent regions. Remarkable low Vs anomalies at shallow depth of 1–5 km are revealed in our model, which are highly consistent with the distribution of sedimentary basins, indicating that the joint inversion of Rayleigh wave phase velocity and Z/H ratio could provide excellent constraints for structure at shallow depth of the TNCO.

2. Data

The ChinArray project aims to obtain high-resolution seismic images of the Earth's lithosphere of Mainland China in order to understand lithosphere deformation and to assess earthquake hazard by deploying a dense transportable array of broadband seismometers across China in multiple phases under the leadership of the Institute of Geophysics,

China Earthquake Administration. In our study, we use the continuous data from the Phase III deployment of the ChinArray. More than 300 portable broadband seismic stations were installed in the TNCO and adjacent regions with an average station spacing of about 30–50 km, covering the east part of the Ordos Basin, WSRS, Luliang and Taihang mountains, and a part of the western NCB (Fig. 1). Each seismograph was equipped with a Guralp CMG-3T seismometer and a Reftek-130 digitizer with a sampling rate of 100 samples per second (sps). Rayleigh wave phase velocities and Z/H ratios are extracted from empirical Green's functions computed from ambient noise data of 306 temporary stations recorded between 01/01/2017 and 07/28/2017.

We follow the procedures of Li et al. (2016) to process the daily continuous ambient noise data of 3 components for each station. We first remove the instrument response, mean and trend from the daily records, which are further down sampled to 1 sps (Bensen et al., 2007). Then the temporal normalization and spectral whitening are applied to the three-component records of each station. To retain the amplitude ratios of vertical and horizontal components, we implement the temporal normalization and spectral whitening following Lin et al. (2014). First, a bandpass filter is applied to 3 components of each station to extract the strongest surface wave signal. Second, we calculate the temporal normalization function with a running-absolute-mean method (Bensen et al., 2007). Third, the unfiltered 3 components records are divided by the maximum of the temporal normalization functions to suppress earthquake signals. Similarly, the spectrum of each record is divided by the average of smoothed spectrums of 3 components to implement the spectral whitening. Finally, 9 noise cross-correlation functions (NCFs) ZZ, ZN, ZE, NZ, NN, NE, EZ, EN, and EE are calculated for each station pair. The 9 NCFs form a 3 by 3 tensor known as the cross-correlation tensor (CCT).

3. Methods

3.1. Phase velocity measurement

We extract phase velocity dispersion curves of Rayleigh wave from ZZ CCFs. For improving signal-to-noise ratios (SNRs) of the Rayleigh wave arrivals, we employ a two-step strategy to stack the daily ZZ CCFs. We first sort the daily NCFs in chronological order and linearly stack them every 5 days to created 5-day stacks of NCFs. We further stack these 5-day NCFs using the time-frequency phase weight stacking (tf-PWS) method (Li et al., 2018a), which has been shown to be more effective in improving SNR than linear stack and meanwhile does not distort the dispersive characteristic of the stacked waveform. We follow Bensen et al. (2007) and define SNR for each period as the ratio of peak amplitude of the signal window to the root-mean-square amplitude of the noise window which is set as the 500-s records after the signal window. The causal and acausal segments of each NCF are summed to further improve the SNR. We then perform the automated frequency-time analysis (FTAN) (Levshin and Ritzwoller, 2001) to calculate the dispersion curves in the period range of 6–40 s for all station pairs that satisfy the far-field approximation (distance between station pair is set to be longer than three wavelengths) (Bensen et al., 2007). To ensure reliable phase velocity measurements, we discard the NCFs with a SNR less than 20. We then conduct an initial 2-D phase velocity tomography for periods of 6–40 s on a 0.25 × 0.25-degree spatial grid covering the study area using a linear ray-theory based tomographic method (Barmin et al., 2001). The histograms of data misfits after the initial tomography are presented in Fig. S1. Referring to the criteria employed by Guo et al. (2016) and our data misfits' distribution, we discard the data with a misfit of more than 6 s. Then we perform the second tomography with the well quality-controlled dispersion curves, which are shown in Fig. S2. Finally, we obtain phase velocity dispersion curves for periods of 6–40 s for each station by taking the value from its closest grid. In the 2-D tomography, we also compute the spatial resolution (Fig. S3), which is defined as twice the standard deviation of the 2-D Gaussian fit to the resolution surface at each grid (Levshin et al., 2005). To further obtain the uncertainties of the phase velocity measurements, we follow the procedure by Shen et al. (2016) to scale the resolution to uncertainty (Fig. S4).

3.2. Z/H ratio measurement

For Z/H ratio measurements, we first linearly stack the daily CCTs of each station pair, and then rotate the nine components to obtain the ZZ, ZR, RZ and RR NCFs using the rotation matrix defined by Li et al. (2016). Theoretically, the ZZ and ZR NCFs are related to the Green's functions of Rayleigh wave as a vertical and a radial record from a vertical source. Likewise, the RZ and RR NCFs are related to the Green's functions of Rayleigh wave as a vertical and a radial record from a radial source. The relative amplitudes of the two NCFs should be retained on account of that we applied the same temporal normalization and spectrum whitening processing to the noise records. Therefore, the Z/H ratios calculated from a vertical and a radial source should be equal. Following Li et al. (2016), the Z/H ratio could be calculated by the equation:

$$\mathrm{E(T)} = \frac{A_{ZZ}}{\mathrm{A}_{ZR}} = \frac{A_{RZ}}{A_{RR}} = \frac{A_{[H(ZZ)+RZ]}}{A_{[H(ZR)+RR]}}. \quad (1)$$

Here E represents the measured Z/H ratio, T represents period, and A represents the maximum amplitude. H is the Hilbert transform which is used here to convert the NCFs to the same phase since there is a 90° phase shift between the ZZ (ZR) and RZ (RR) NCFs. Examples of ZZ, ZR, RZ, RR NCFs of two stations 14842 and 13801 are shown in Fig. S5.

We closely follow the algorithm from Tanimoto and Rivera (2008) to estimate the Z/H ratios. More specifically, we first employ Gaussian band pass filters with different bandwidths to filter the stacked Z and R records. The bandwidths of the filter depend on both the central frequencies and the distances between sources and receivers (Herrmann, 1973). Then we compute the zero-lag cross-correlation coefficient for them and discard the station pairs that have coefficients lower than 0.8. Finally, we compute the envelope functions for the filtered records and calculate the ratio of their maximum amplitudes for the final Z/H ratio measurements. To obtain the most reliable measurements, we adopt multiple quality control criteria to discard the measurements of stations that might have misorientation or other factors that lead to unreliable measurements. First, we discard any records with a SNR of either the Z or R component <8. Second, we choose station pairs with an interstation distance greater than 3 wavelengths. Third, we require at least 20 individual measurements that exhibit a Gaussian distribution with standard deviation less than 15% of the average to obtain a robust average of the Z/H ratio at a station. And stations with less than 5 robust Z/H ratio measurements are further discarded.

To further ensure the reliability of the measurements, we also measure Z/H ratios from earthquake data recorded between November 2016 and January 2019. We select about 700 events with moment magnitudes greater than 5.5, focal depths less than 100 km, and epicentral distances between 10° and 140° (Fig. S6). We first remove the instrument response, linear trend and mean and cut out the Rayleigh wave from each record. Then we apply a 5–50 s bandpass filter to each record and decimate it to 1 sps. The horizontal components are further rotated to radial and transverse directions to compute Z/H ratio at periods of 10–40 s. The detailed procedures and criteria for calculating Z/H ratios from earthquake data are similar to those for ambient noise.

3.3. Joint inversion

For each station, we jointly invert the phase velocity and Z/H ratio data to obtain a 1-D velocity model by using a Bayesian Markov chain Monte Carlo (MCMC) method, which is implemented with a DRAM (Delayed Rejection Adaptive Metropolis) algorithm (Li et al., 2016). The DRAM algorithm is used to improve the MCMC by increasing the probability of sampling regions with higher posterior probability. This is

done by updating the acceptance probability of the new candidate model on a regular interval that is determined by previous samples in the chain. More details about DRAM can be found in published works such as Haario et al. (2006) and Mira (2001). Since the joint inversion has been widely used and well described by the previous studies (Bodin et al., 2012; Shen et al., 2013; Li et al., 2019), we will not elaborate the details here.

In this study, we parameterize the 1-D velocity model beneath each station as three layers, consisting of a sedimentary, a crystal crustal, and an upper mantle layer. The sedimentary layer is parameterized by four variables: sedimentary thickness and S wave velocities at the upper boundary and lower boundary, and the average V_p/V_s ratio in the sediments. We constrain the S wave velocity and average V_p/V_s ratio ranges in the sedimentary layer referring to a previous study (Li et al., 2019). And the S wave velocity in the sedimentary layer is set to increase linearly. The crust is constrained by 4 cubic B-splines for V_s and a Moho depth. Similarly, another four cubic B-splines are used to describe the V_s of the upper mantle layer. Overall, we have 13 independent parameters that are set to perturb within certain ranges to invert the 1-D Vs model. We utilize the Crust 1.0 global model (Laske et al., 2013) for initial sedimentary thickness. The initial Moho depths are obtained from Wang et al. (2017) and Li et al. (2018b). We perturb sedimentary thickness by ±2 km and Moho depth by ±5 km from their initial values. Considering that the sedimentary thickness of the Crust 1.0 model is not accurate enough, we take the sediment thickness of the inverted model and use it as the initial value for the second inversion. We employ the PREM model (Dziewonski and Anderson, 1981) as the initial Vs model in the depth range of 0–200 km with a searching range of ±20%. Vs below 200 km depth is set as constant from PREM model. Note although we invert Vs down to a depth of 200 km, we expect the most resolvable depth range to be 0–50 km as the longest period of the data we use is 40 s. We also assume the velocity model to be isotropic. The thickness of sedimentary and crustal layer is unknown and is inverted simultaneously. The forward modeling is performed with the MINEOS package (Masters et al., 2007). Following Li et al. (2016), the joint misfit function is defined by

$$M_{JOINT} = c_1 \bullet M_{SW} + c_2 \bullet M_{ZH} = c_1 \bullet \sum_{i=1}^{N} \frac{\left[G_i(m) - D_i^{obs}\right]^2}{\sigma_i^2} + c_2 \bullet \sum_{j=1}^{M} \frac{\left[\mathrm{R_j(m)} - \mathrm{B_j^{obs}}\right]^2}{\gamma_j^2}. \quad (2)$$

Here $G_i(m)$ represents the phase velocity of period i calculated from model m, and D_i^{obs} represents the observed phase velocity of period i. Similarly, $R_j(m)$ represents Z/H ratio of period j calculated from model

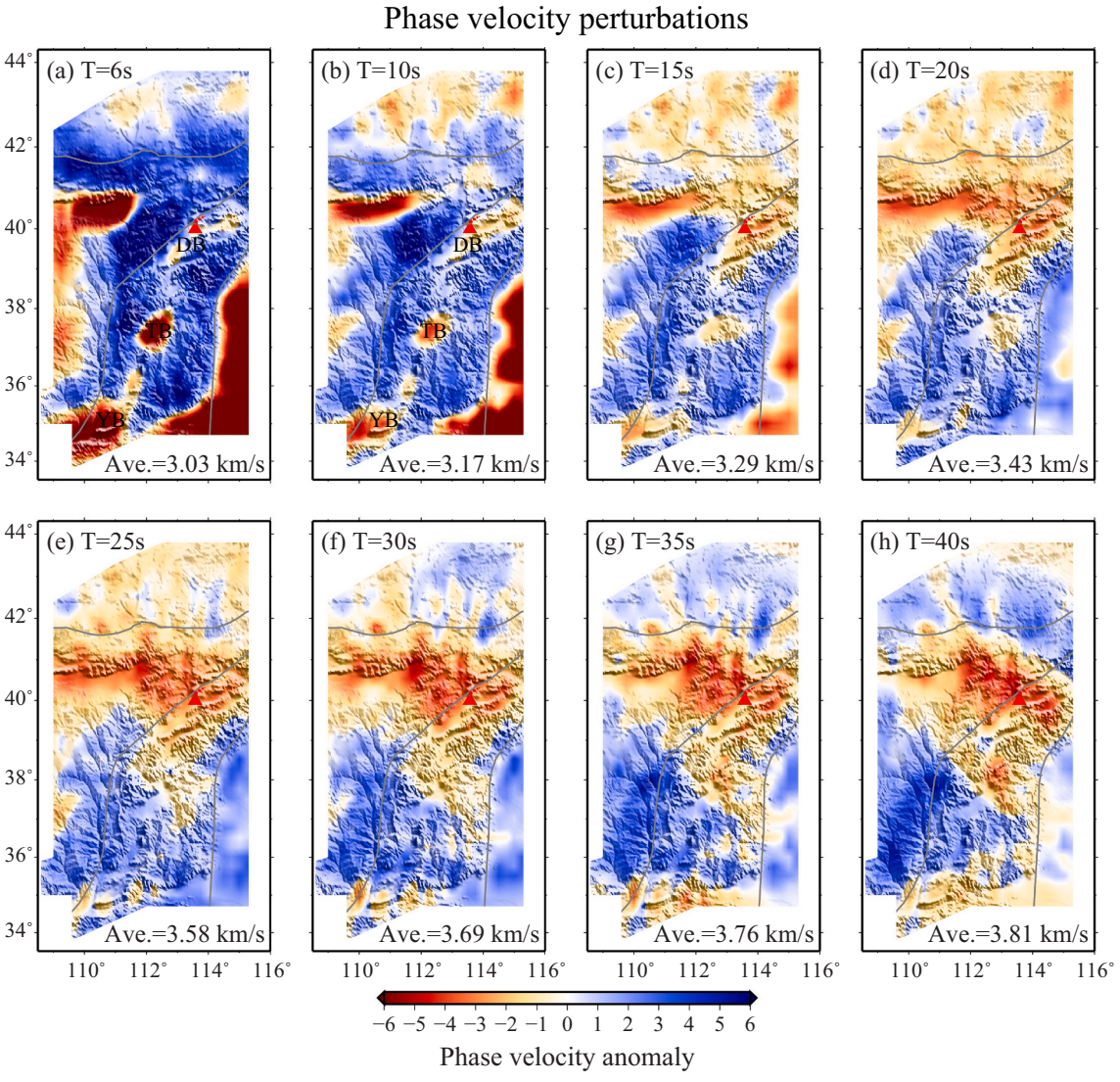

Fig. 2. Maps of phase velocity anomaly for different periods from 6 s to 40 s. The average velocity of each period is marked at the lower right. DB: Datong Basin; TB: Taiyuan Basin; YB: Yuncheng Basin.

m, while B_j^{obs} represents the observed Z/H ratio of period j. N and M are the numbers of periods for phase velocity and Z/H ratio, respectively. σ_i and γ_j are, respectively, the uncertainties of phase velocity and Z/H ratio. c_1 and c_2 represent the weighting coefficients, which are set to be the same in this study ($c_1 = c_2 = 0.5$).

For each station, 100,000 shear wave velocity models are generated by the Markov Chain Monte Carlo sampling of model space constructed by the reference model mentioned above, and their misfits are calculated according to Eq. (2). By averaging the selected 3000 accepted models that have the lowest misfits, we estimate the final 1-D Vs model for each station.

4. Results

4.1. Rayleigh wave phase velocity maps

Rayleigh wave phase velocity anomaly maps for periods of 6–40 s are presented in Fig. 2. Rayleigh phase velocity for 6–10 s (Fig. 2a, b) is mainly sensitive to the Vs of upper crust, which exhibits good correlation with surface geology. Low phase velocity anomaly is observed in basins with thick sediments, including the Ordos Basin, NCB, Datong Basin, Taiyuan Basin and Yuncheng Basin. The WSRS and Hetao graben also show low phase velocity anomaly as well. Meanwhile, the mountains, such as the Luliang Mountains, Taihang Mountains and Yinshan orogenic belt are featured by high phase velocities. In the medium period band (15–20 s, Fig. 2c, d), a large-scale low phase velocity anomaly appears beneath the Datong volcanic region, which gradually

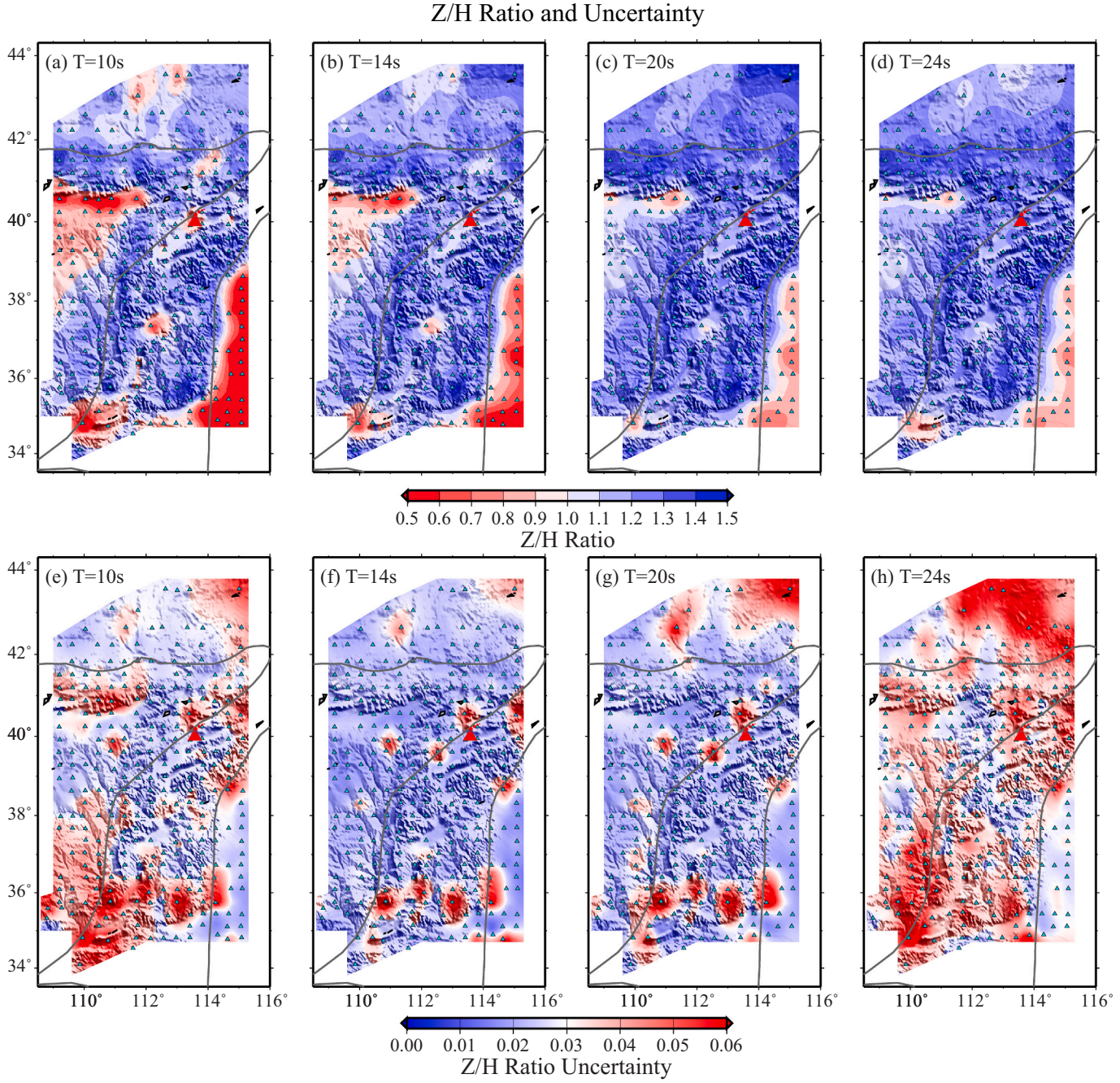

Fig. 3. (a–d) Z/H ratios for 4 different periods (10 s, 14 s, 20 s, 24 s). (e–h) The corresponding uncertainties for the Z/H ratios for periods of 10 s, 14 s, 20 s and 24 s.

expands as periods increase and become connected with the low phase velocity anomaly beneath the northeast end of the Ordos Basin and Hetao graben. We also find that low phase velocity beneath NCB starts to become high at this period band. While the northern WSRS remains as a low phase velocity region, the southern part of the rift system evolves into a high velocity section. At longer periods (Fig. 2e, h), the low velocity anomaly beneath the Datong volcanic complex continues expanding to the west. The Ordos Basin is characterized by high phase velocities, which appears to extend to the southern segment of the rift.

4.2. Z/H ratio maps

An example of the histograms of Z/H ratios at 18 s measured from ambient noise and earthquake data for station 14811 is presented in Fig. S7, both of which exhibits an approximately normal distribution. We use the averages and 1.5 times of standard deviations (σ) as the estimated Z/H ratios and uncertainties, referring to the theory by Lin et al. (2009), which suggests using 1.5σ as uncertainty of systematic and random measurement errors. We calculate the differences between the Z/H ratio measured from ambient noise and earthquake surface wave, respectively. The statistical histograms of the Z/H differences for different periods are presented in Fig. S8. The Z/H ratio measurements with error bars of six stations from ambient noise and earthquake data are presented in Fig. S9. In most cases, the Z/H ratio measurements from ambient noise and earthquake data agree well with each other except for few stations. An example is station 15799 (Fig. S9f), where the measured Z/H ratios from ambient noise and earthquake data are significant different. We notice that such discrepancy has been reported by previous studies (Li et al., 2016; Xu et al., 2020) while its cause(s) are still unknown. Here we simply discard these stations from the final Z/H dataset, which consists of 295 Z/H ratio measurements for the joint inversion.

Fig. 3 shows the measured Z/H ratios at four different periods (10 s, 14 s, 20 s, 24 s) and their corresponding uncertainties. For each period, triangles in light blue indicate the stations that have robust measurements to interpolate for the 2-D maps. Almost all the basins and rifts, except for the southern part of Ordos Basin, are characterized by a low Z/H ratio at all periods. The mountainous regions, on the other hand, generally have high Z/H ratios. The contrast fades away as period increases. At 10 s and 24 s, the uncertainties of some Z/H ratio measurements are relatively large but at 14 s and 20 s most uncertainties are very small.

4.3. 1-D velocity profiles

For each station, a 1-D Vs model is jointly inverted from the measured phase velocities and Z/H ratios. Fig. 4 shows the inverted 1-D velocity profiles at two stations 14855 and 13840, which are located at the Taihang Mountains and NCB (blue triangles in Fig. 1), respectively. We also show the observed and computed phase velocities and Z/H ratios at these two stations. At short periods, the observed phase velocities at station 13840 located inside NCB are much lower than those measured at 14855 at the Taihang Mountains. The measured Z/H ratios of these two stations also exhibit a similar feature. Furthermore, the whole Z/H ratios at all periods of station 13840 are lower than station 14855. It indicates a thicker sedimentary layer beneath station 13840, which is consistent with the geological setting of the station. The inverted 1-D shear wave velocity models shown in Fig. 4a and b show very different characteristics. Shear wave velocity at shallow depth beneath station 13840 is much lower than that of station 14855. Furthermore, we inverted the 1-D Vs models for the two stations without and with Z/H ratio added in the inversion (Fig. S10), proving that the Z/H ratio can provide better constraints on the shear wave velocity of the shallow structure for stations located in regions with or without thick sediments.

4.4. 3-D shear wave velocity model

After the 1-D shear wave velocity models beneath all stations are obtained after the inversion, they are interpolated to a 0.25° × 0.25° grid with a minimum curvature surface-fitting method (Smith and Wessel, 1990). The final 3-D Vs model covers roughly from 108.5°E to 116.0°E in longitude, 33.5°N to 44.3°N in latitude and 1 to 50 km in depth. Fig. 5 presents a series of horizontal slices of the model at different depths (1, 3, 5, 10, 15, 30, 40, and 50 km).

In the 1, 3, 5 km depth slices (Fig. 5a–c), there is a clear correlation between the Vs and near-surface geological settings. Extremely low Vs is observed beneath the basins and rifts, including the Ordos Basin, Hetao graben, Shanxi Rift, Weihe Rift, Taiyuan Basin, Datong Basin and NCB. The low amplitude of Vs can be attributed to sediments in these regions. Meanwhile, the Luliang, Taihang and Yinshan mountainous regions are characterized by high amplitude of Vs. The boundaries between high and low velocity zones are distinct and correspond well with the edges of sedimentary basins and rifts. In particular, the narrow low Vs band corresponding to the WSRS is well resolved due to the dense station coverage. The advantage of Z/H ratio for constraining shallow crustal structures is well presented in this study.

Fig. 6a presents the 2-D distribution of sedimentary thickness of the study region obtained by this study. For comparison, we also show the sediment thickness distribution of the Crust1.0 model (Fig. 6b). It is obvious that our model has higher resolution and better relevance to surface geological settings. In our model, the Hetao graben, Ordos Basin, Weihe Rift and NCB are covered by a particularly thick sedimentary layer, with a maximum thickness of over 4 km. Our study area covers the eastern part of the Ordos Basin, which exhibits a significant variation in sediment distribution. In general, sediment thickness gradually increases from southeast toward northwest. Along the WSRS, the mapped sediment cover is also highly heterogeneous with large distributions along the three basins within in the system, the Datong Basin, Taiyuan Basin and Yuncheng Basin from north-northeast to south-southwest. On the other hand, the inverted sediment thickness in the orogenic regions (Taihang, Luliang and Yinshan Mountains), is almost negligible.

The large variations in sediments infills in the study area is also clearly illustrated in cross sections (Fig. 7). The positions of these cross sections are indicated in Fig. 6a. The E-W section A-A' extends from the Hetao graben to area near the Datong Basin, revealing the thickness of sediments beneath these tectonic units. It is about 4 km thick in the Hetao graben and decreases to almost zero when it reaches to the Taihang orogenic belt. Section B-B' is an E-W profile along latitude 37.3°N and runs across three sedimentary basins: Ordos Basin, Taiyuan Basin and NCB. Sediments in the Ordos Basin is relatively thin and diminishes toward east. Sediments infills inside the Taiyuan Basin and NCB in the middle and eastern part of the profile are more prominent, reaching nearly 3 km in most parts. Similarly, section C-C' runs in the E-W direction through the Weihe Rift and NCB, showing a sediment infill of 3 km and 5 km thick beneath the rift and basin, respectively. We also present two sections, D-D' and E-E', to illustrate changes in sedimentary distribution along the N-S direction. Section D-D' in the western part of this study area extends from the Yinshan Mountains in the north to the Weihe Rift in the south and runs across the eastern Ordos Basin. It shows a gradual thinning of sediment cover beneath the Ordos Basin from north to south. At the southern end of the profile, the Weihe Rift processes a thick sedimentary layer that reaches nearly 4 km. The east profile E-E' runs across the Yinshan orogenic belt in the north and the west edge of the NCB, showing an over 5 km thick sedimentary layer beneath the NCB. We also take an NNE-SSW profile F-F' which roughly samples the WSRS. Sedimentary infills of the three basins from NNE to SSW are approximately 1.5 km, 3 km, and 4 km in the Datong Basin, Taiyuan Basin and Weihe Rift, respectively, suggesting an increase of sedimentation from north to south. We also present the uncertainty of the sedimentary thickness in Fig. S11 to evaluate the accuracy of the jointly inverted results, which shows that the uncertainty is related to

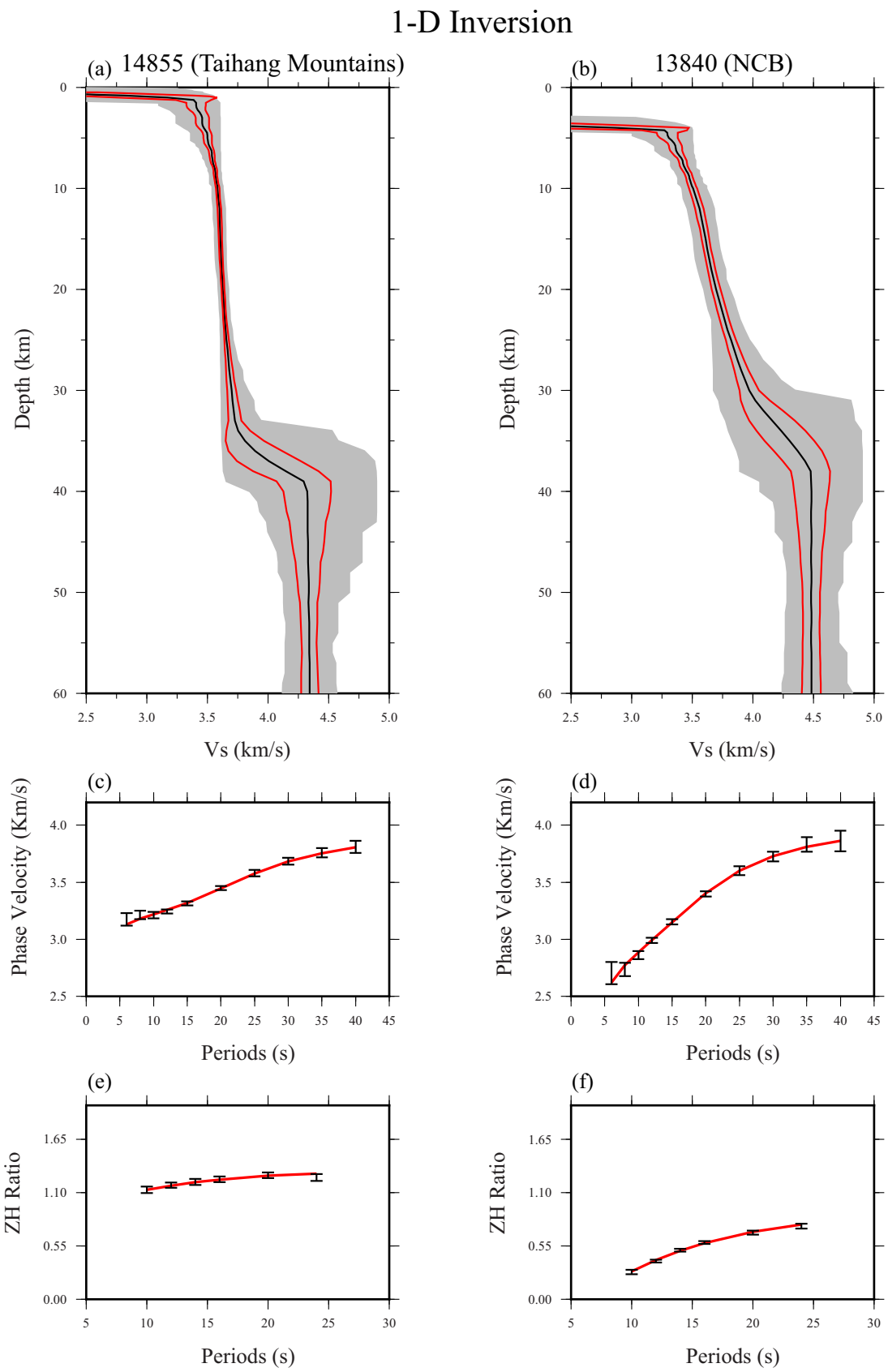

Fig. 4. Joint inversion results of phase velocity dispersion curves and Z/H ratios for 1-D models of station 14855 which located in Taihang Mountains and station 13840 which located in NCB (triangles in blue shown in Fig. 1). (a, b) The averaged 1-D Vs models (black lines) for the two stations 14855 and 13840 with one standard deviation perturbations (red lines) and posterior distributions (gray shaded regions). (c, d) Observed surface wave dispersion curves (black error bars) and predicted surface wave dispersion curves (red lines) from the joint inversion. (e, f) Same as (c, d) but for Z/H ratios. (For interpretation of the references to colour in this figure legend, the reader is referred to the web version of this article.)

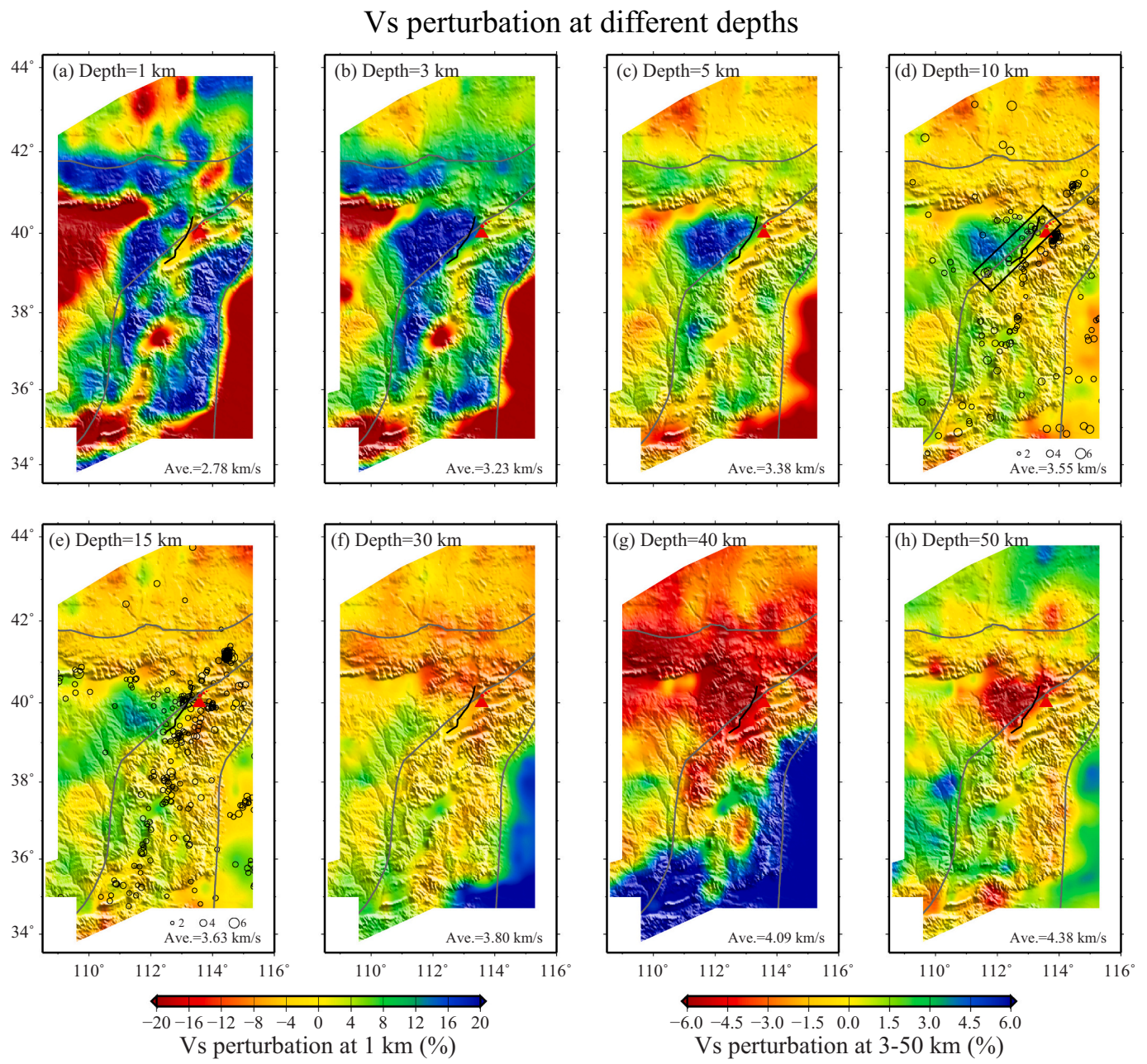

Fig. 5. Maps of Vs perturbation at different depths (1–50 km) obtained from joint inversion of phase velocity dispersion curves and Z/H ratios, with the average Vs shown at the lower right. The black circles in (d, e) delineate the earthquakes ($M_L \geq 2.5$) from 1987 to 2016 in the study area. The black line in the west side of the Datong volcanic complex indicates the Kouquan Fault.

the inverted sedimentary thickness. It can be observed that the uncertainty is very small where the sediments are relatively thin. The uncertainty is relatively larger where the sediments are very thick, but is still less than 1 km. It indicates that the lateral variations of the sedimentary thickness we discussed are reliable.

Slices of Vs at 10–15 km depth (Fig. 5d–e) are related to structure of middle crust. In the middle crust, low velocity anomalies are mainly concentrated around the WSRS, Hetao graben and NCB. Another noticeable low velocity region is the area around the Datong volcanic complex, extending eastward from the Datong Basin to the northernmost part of Taihang orogenic belt and westward to the Yinshan orogenic belt. On the other hand, the Ordos basin, the Luliang and northern Taihang orogenic belts generally are featured by relatively high S-wave velocity. What is worth noting is that the northeast end of the Ordos Basin shows significant high velocity anomaly in upper and middle crust. The Vs structures of the lower crust at 30–40 km are shown in Fig. 5f and g, which appears to be quite different from those of the middle crust. The orogenic belts turn into low velocity zones while the NCB changes to an extremely high velocity region. The central to southern parts of Shanxi Rift gradually convert to high velocity areas. For the major part of the Ordos Basin, the high Vs structure seen in the middle crust remains in the lower crust. The difference is that as the depth increases, the high velocity structure in its northeast end is gradually replaced by a large scale LVZ connecting the Datong volcanic complex. The LVZ around Datong volcanic complex still exist and its range expands with depth. Furthermore, the center of the LVZ around Datong volcanic complex gradually shifts to the west. In the uppermost mantle, shown in slice at 50 km depth (Fig. 5h), the prominent LVZ near Datong volcanic complex shifts to the northeast end of the Ordos Basin. The Yinshan orogenic belt and the north part of Luliang, Taihang orogenic belts remain as low Vs

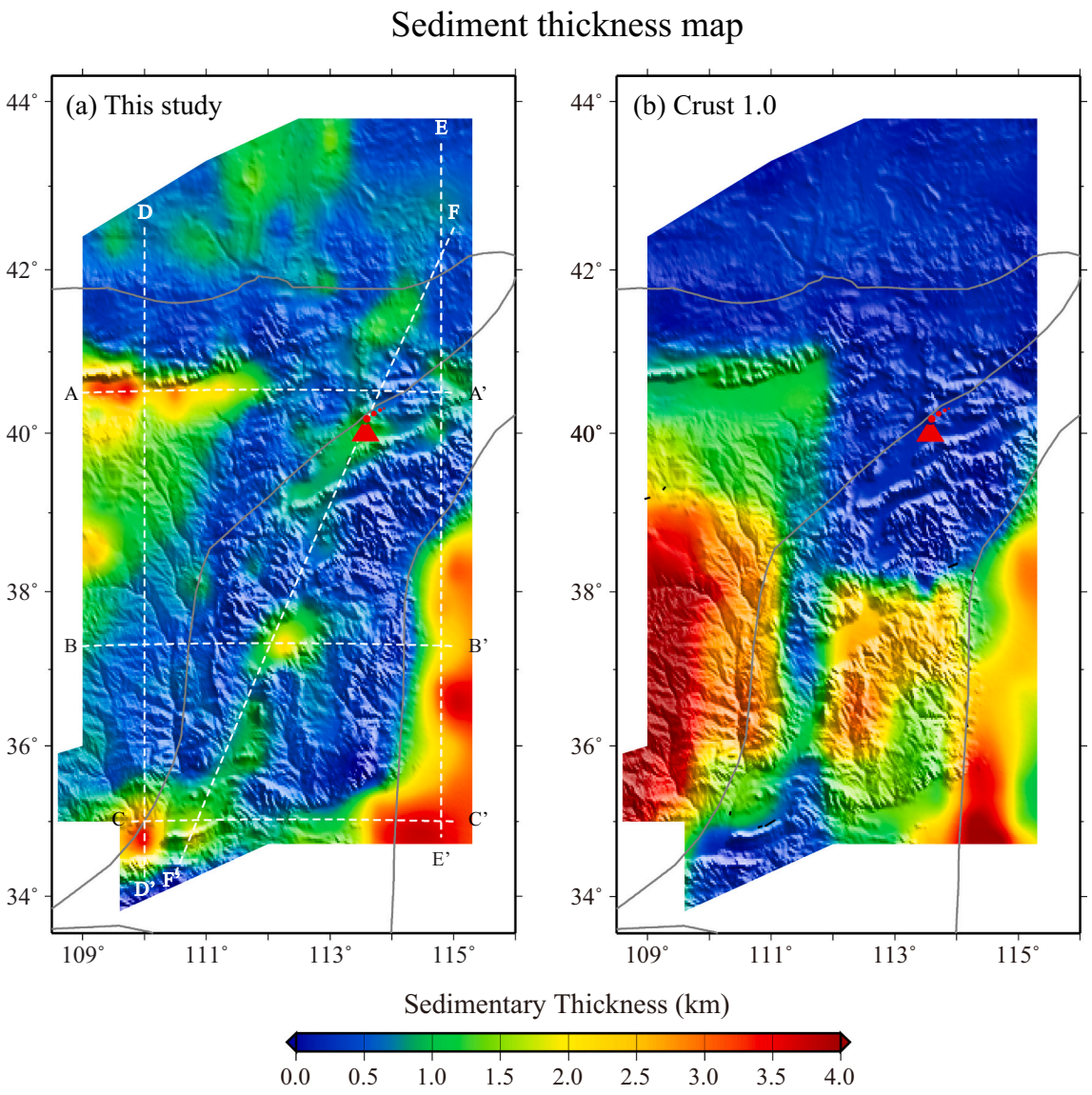

Fig. 6. (a) Sedimentary thickness calculated by joint inversion of Rayleigh wave phase velocity dispersion curves and Z/H ratios in this study. The white dashed lines depict the locations of the vertical profiles presented in Fig. 7. (b) The sedimentary thickness obtained from the Crust1.0 model.

regions, forming a large scale LVZ including the northeast end of the Ordos Basin and Datong volcanic complex. The NCB remains as a high Vs region. The high velocity anomaly in Ordos Basin gradually extends eastward and reaches the southern TNCO.

5. Discussion

5.1. Comparison with previous published models

Li et al. (2018b) obtained a Vs model of the northern Ordos Basin by surface wave tomography from ambient noise phase velocity and teleseismic data. Ai et al. (2019) built a Vs model of the Weihe Rift system by a joint inversion of receiver function and ambient noise phase velocity data. Our study area shares partly with these two studies. In general, our Vs model agrees with their results, especially in the deep part. Since their methods focus more on the deeper structure of the crust and upper mantle, the resolution on shallow (< 5 km) Vs structures is generally insufficient. Xu et al. (2020) presented a Vs model of Shanxi Rift by a joint inversion of Rayleigh wave phase velocity and ellipticity data, which is similar to our study.

One major difference between previous and our models is the lateral resolution due to the density of data. All the previous study used the provincial seismic networks of the China Earthquake Administration (CEA) or a smaller array. These networks have a highly uneven station distribution with an average station interval two to three times larger than the ChinArray. The difference in lateral resolution might contribute to discrepancies among different models. For example, model of Li et al. (2018b) showed a roughly punctiform low velocity anomaly beneath Datong volcanic complex at a depth of 10 km (fig. 10a in Li et al., 2018b). While in our model, the low velocity anomaly beneath Datong volcanic complex at the same depth exhibits banded distribution along the strike of Shanxi Rift (Fig. 5d). The model of Xu et al. (2020) showed that the Datong Basin had the thickest sediments in the Shanxi Rift. However, our model exhibits different feature that the sediments in southern and central Shanxi Rift are thicker than that in the northern part, which is consistent with the results of geological research (e.g., Zhang et al., 1998). Moreover, the sedimentary basins within the TNCO are better constrained in our model. For instance, in the model of Xu et al. (2020), the sediments related low Vs in Datong Basin showed a strong smearing effect that spread across the northeastern Ordos Basin due to low spatial resolution. And the low Vs related Taiyuan basin appeared to be misplaced slightly to the northeast.

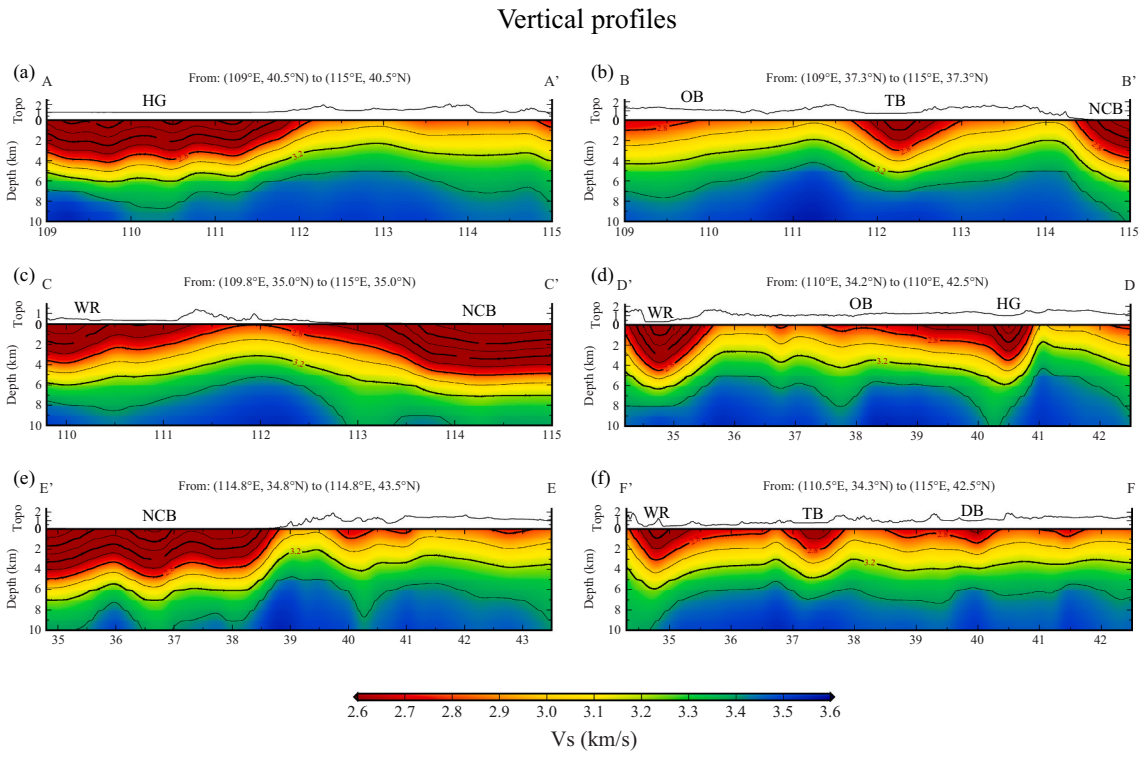

Fig. 7. Vertical sections (1–10 km depth) of the 3-D shear wave model from joint inversion. The locations are depicted in Fig. 6a. The topography along the sections are presented at the top. HG: Hetao graben; OB: Ordos Basin; NCB: North China Basin; WR: Weihe Rift; DB: Datong Basin; TB: Taiyuan Basin.

5.2. Sedimentary thickness and its tectonic implications

The thick sedimentary layers in Hetao graben, northern Ordos Basin and NCB, locally exceeding 4 km, are roughly consistent with previous study by receiver functions (Wang et al., 2017) and deep seismic sounding (Teng et al., 2010; Wang et al., 2014b), but are of higher resolution in our study. NCB is generally regarded as an extensional basin, which received a large amount of Cenozoic sedimentation (Tang et al., 2011). Our model provides evidence for this from seismic imaging with high resolution. As for the Ordos Basin, previous geological studies proposed that the Ordos Basin went through three stages of evolution, that is, the stage of differential rise and fall in early Paleozoic, the stage of whole tilting during late Paleozoic and Mesozoic, and the stage of development of faulted basin in Cenozoic (Deng et al., 2005). These long-term and complex geological tectonic evolution can be reflected in shallow sediments. In our model, the thickness of sedimentary layer in the Ordos Basin exhibits remarkable heterogeneity. For example, the difference in the east-west direction coincides well with previous deep seismic sounding study (Wang et al., 2014b): a thicker sedimentary layer in the west and thinner one in the east, which could be caused by whole-block tilting during Late Paleozoic and Mesozoic and the afterward intense erosion in the eastern Ordos Basin since Late Cretaceous (Deng et al., 2005; Liu et al., 2006).

There are also thick sedimentary layers observed in the faulted basins around the Ordos Basin, including Hetao graben, Taiyuan Basin and Yuncheng Basin, which are likely related to Cenozoic sedimentation (Zhang et al., 1998). As mentioned above, previous geological studies suggested that during the Oligocene-Pliocene rifting started from the Weihe Rift and extended to the Shanxi Rift (Zhang et al., 1998). But it still lacks large-scale seismic image evidence that cover the whole WSRS. With the high-resolution Vs model developed here, this can be supported by the feature of sedimentary thickness in our result that it gradually decreases from south to north in the WSRS. The sediments in the Weihe Rift are the thickest while in the northernmost part of Shanxi Rift (Datong Basin) are the thinnest. Previous studies based on borehole, receiver function and surface wave data (e.g., Zhang, 2000; Wang et al., 2017; Xu et al., 2020) showed different sedimentary thicknesses at some locations compared with our results. For instance, sedimentary thickness in the Datong Basin are over 2 km based on their works, while in our model it is ~1–2 km (Fig. 7f), which is roughly consistent with the result (~0.6–2 km) by Zhang et al. (1998). This might be because the results from boreholes and receiver function are likely to represent specific structures at certain locations while our model derived from surface wave is more likely to reflect regional structures on a larger scale. The difference between the model by Xu et al. (2020) and ours could be caused by the different array distributions as we mentioned in Section 5.1. Moreover, geological research (e.g. Zhang et al., 1998) revealed that the sediments subsidence in the Weihe Rift started in the mid-late Eocene and the sediments subsidence in the central and northern Shanxi Rift started in the late Neogene. Therefore, it could be inferred that the sediments of the southern WSRS are thicker and older than that in the north, indicating that the WSRS has likely propagated from south to north (Zhang et al., 1998). Hence, our model with high resolution at shallow depth provides an unprecedented seismic evidence for the expanding direction of the WSRS.

In our model, the WSRS is underlaid by a low Vs across the entire range in the upper and middle crust, only the north segment, which houses the Datong volcanic complex, exhibits a substantial low velocity structure in the lower crust and the uppermost mantle. It indicates that the rifting in the northern section is more significant than that in the southern section at present, which is consistent with the active volcanism in the northern section. Below the middle crust, the southern end of the LVZ beneath WSRS is located roughly at the middle of the rift system (Fig. 5e–h). This suggests that the magmatism does not spread to the southern segment of the WSRS. Besides, considering the south-to-north propagation of the WSRS evidenced by our sediments model, the evolution of the WSRS is unlikely to be controlled by the active mantle welling from the north. On the contrary, the rifting in the WSRS is more likely to be controlled by the counterclockwise rotation of the Ordos Basin driven by the lateral expansion of the northeastern Tibetan

Plateau from the south (Li et al., 2005). Overall, our results suggest that the rifting of WSRS is likely to propagate from south to north, controlled by the uplift of the Tibetan Plateau, and is more active in the northern segment at present.

Moreover, the 2-D high-resolution map of sedimentary thickness in our model provides quite accurate constraints for shallow crustal structure for future study of deeper structure in the study area. For instance, the sediment reverberations could affect the extraction of receiver functions of stations located at basins with thick sediments because the P to S conversions are weaker and likely obscured by the sediment reverberations (Sheehan et al., 1995). With an accurate sediment model, we could remove the sedimentary reverberations from seismic records and obtain robust receiver functions for studying deeper structure.

5.3. Crustal and uppermost mantle heterogeneities in different parts of the NCC

Our 3-D shear wave velocity model covers the whole TNCO, eastern Ordos Basin, and a western part of NCB, offering high resolution images to compare and investigate the lateral heterogeneities of the crustal and uppermost mantle structure of the three different tectonic units. The eastern part (NCB) next to Taihang Mountains covered in this study, exhibits relatively homogeneity within its interior but completely different characteristics of Vs structure from the Ordos Basin and TNCO. Low velocity anomaly is observed beneath NCB from upper crust to middle crust. Whereas it turns to high velocity anomaly at 30 km depth, which is likely due to a shallow Moho revealed by previous studies (e.g., Zheng et al., 2009; Bao et al., 2013; Guo and Chen, 2017). The low velocity anomaly in the shallow depth is related to the thick sediments in the NCB, while the low velocity anomaly in the middle crust should result from a hot crust since the heat flow value of NCB is pretty high (Hu et al., 2000). The thinned and hot crust beneath NCB support extensional tectonism and indicates that NCB might be still in thermotectonic activation (Zheng et al., 2009; Tang et al., 2013). The Ordos Basin, widely believed to preserve a cratonic keel during the destruction of the NCC in the Mesozoic and Cenozoic (Griffin et al., 1998; Menzies et al., 2007; Chen et al., 2014), generally exhibits relatively high Vs in the middle crust and uppermost mantle inside the block. Nevertheless, the TNCO is characterized by strong lateral heterogeneity in the whole crust and uppermost mantle, which indicates that the TNCO might have experienced complicated evolutionary process since its formation resulting from the amalgamation of the eastern and western NCC at ~1.85 Ga (Zhao et al., 2005).

5.4. Crustal upwelling channel and origin of Datong volcanism

A conspicuous feature of our model is the remarkable LVZ beneath the Datong volcanic complex and its adjacent region, extending from the middle and lower crust to the uppermost mantle. Similar LVZs beneath this region have also been found in previous seismic studies (Huang and Zhao, 2006; Zhao et al., 2009; Lei, 2012; Tang et al., 2013; Li et al., 2018b), which are generally attributed to the Datong volcanism. The Neogene basaltic outcrop widely distributed around this region (Liu et al., 2004; Xu et al., 2005) also provided relevant evidence for that. As mentioned above, the dynamic mechanism and origin of Datong volcanism is still disputed. Our model exhibits that as the depth increases, the horizontal range of the LVZ expands in the lower crust and reduces in the uppermost mantle (Fig. 5f–h), which indicates that the upwelling hot materials from asthenosphere have intruded the lower crust beneath northeastern end of Ordos Basin, Yinshan orogen belt, and even the Hetao graben. The intruding magma heats the lower crust of a large area of the TNCO and causes such wide range low velocity anomaly. However, the LVZ in the middle and upper crust is less intense (Fig. 5c–e), which indicates that the magmatism beneath Datong volcanic complex is likely to be limited below middle crust, which is consistent with that Datong volcanic complex is inactive at present (Xu et al., 2005). Moreover, below the middle crust, the low-velocity structure beneath the volcanic regions extends further deep into the uppermost mantle at a location ~150 km west of the volcanic complex (Fig. 5f–h), which might delineate the crustal upwelling channel of the hot materials from the asthenosphere. The crustal upwelling channel can be better exhibited with the vertical profiles of Vs perturbation in Fig. 8. It can be observed that the upwelling hot materials from asthenosphere beneath the northeastern end of Ordos Basin rise into the middle crust and are blocked by the stable high-velocity upper crust therefore flow eastward and rise to the Datong volcanic complex. Based on our Vs model of the crust and uppermost mantle, we suggest that the vertically continuous low-velocity structure beneath the Datong volcanic complex is likely caused by upwelling asthenosphere arising between the northern and northeastern ends of the TNCO and Ordos Basin, respectively. It is worth noting that the northeast end of the Ordos Basin exhibits high velocity anomaly in the upper and middle crust but turns into low velocity anomaly in the lower crust and uppermost mantle. Considering the Datong volcanism mentioned above, the significant low velocity beneath the northeast end of the Ordos Basin probably indicates that its lower crust has been heated and even partly melted by the upwelling hot material from the asthenosphere. The relatively deeper Moho beneath this region could represent the underplating or interpenetration under the crust by melted material related to the Quaternary volcanism. Therefore, we propose that the upwelling hot material from the asthenosphere arising between the northern and northeastern ends of the TNCO and Ordos Basin is the origin of Datong volcanism.

5.5. Some implications for seismicity

We collect over a thousand of earthquakes ($M_L \geq 2.5$) in our study area from 1987 to 2016 and find that the dominating magnitude is about M_L 3 and most earthquakes occurred at depth of 10–15 km (Fig. S13). Therefore, we plot the earthquakes within ±2 km at depth of 10 and 15 km in the Vs perturbation slices (Fig. 5d–e). It can be observed that the earthquakes are mainly distributed along the Shanxi Rift and the number of earthquakes in the northern segment are relatively larger than that in the southern segment. This is consistent with our Vs model that the middle crust of the southern segment exhibits higher shear wave velocity, which indicates a relatively more stable middle crust. And according to our model, the low velocity anomaly in the middle crust of northern segment of the Shanxi Rift should be related to the Datong volcanism. Previous study suggested that the low velocity anomaly in the crust may represent high-temperature anomaly or fluid reservoirs that could trigger earthquakes (Zhao et al., 1996). Hence, we suggest that the stronger seismicity in the northern segment of the Shanxi Rift is likely to be related to the Datong volcanism. Moreover, an obvious phenomenon is that many earthquakes are located at the junctions of the

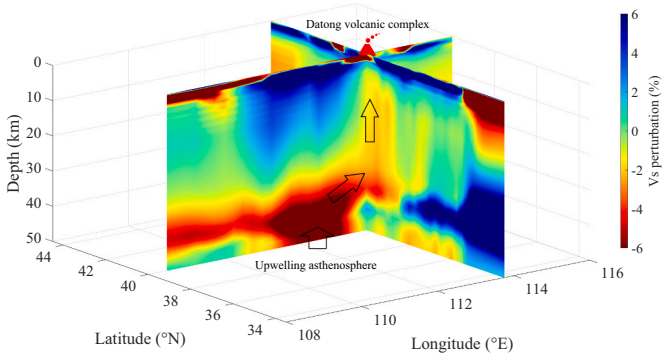

Fig. 8. Vertical sections (1–50 km depth) of Vs perturbation across the Datong volcanic complex (along the warp and weft, respectively). The Vs perturbation is calculated based on the average Vs at each depth presented in Fig. 5.

high velocity anomalies and the low velocity anomalies such as those in the black rectangle in Fig. 5d, which is consistent with the previous inferences (e.g., Hauksson and Haase, 1997; Huang and Zhao, 2004). Therefore, we suggest that more attention about seismic risk should be paid to the large velocity gradient zones in the study area, especially around the northeastern end of Ordos Basin. In addition, the large velocity gradient zone in the black rectangle is the boundary of the Western NCC and the TNCO (Zhao et al., 2005), along which a major fault known as the Kouquan Fault has been developed (shown by black line in Fig. 5). In the Vs slice of 30 km (Fig. 5f), this sharp velocity difference fades off, which might indicate that the Kouquan Fault is likely to extend down to the middle crust but not to the lower crust.

6. Conclusions

We obtain a sedimentary thickness map and a 3-D Vs model with high resolution of the crust and uppermost mantle beneath the TNCO and its adjacent regions by a joint inversion of the Rayleigh wave phase velocity dispersions and Z/H ratios from ambient noise correlation. The shallow Vs anomalies are better constrained due to the combination of Z/H ratios measurements, which exhibit high correlation with the surface geological settings. Our model shows prominent heterogeneities of crust and uppermost mantle in different tectonic units of NCC. The difference of sedimentary thickness and Vs between the southern and northern segments WSRS suggests that the rifting of WSRS is likely to propagate from south to north, controlled by the lateral expansion of the northeastern Tibetan Plateau. Our results also suggest that the northern segment of the WSRS is more active at present, which is manifested by the Quaternary *syn*-rift Datong volcanic complex. The low-velocity structure beneath the volcanic complex extends further deep into the uppermost mantle at a location ~150 km west of the complex, which is speculated for a nearly horizontal channel in the lower crust for the upwelling of the hot materials from the asthenosphere. The upwelling hot material arising from the asthenosphere is located between the northern and northeastern ends of the TNCO and Ordos Basin and is the likely origin of the Datong volcanism. The observed seismicity along the WSRS also suggests that currently the northern segment of the rift system is more tectonically active.

Data availability

Datasets related to this article can be found at https://doi.org/10.17632/9tcj862hrh.2.

Declaration of Competing Interest

The authors declare that they have no known competing financial interests or personal relationships that could have appeared to influence the work reported in this paper.

Acknowledgments

We thank the Data Management Center of China National Seismic Network at Institute of Geophysics, China Earthquake Administration (ChinArray DMC, doi:10.12001/ChinArray.Data) for providing the waveform data. This work was supported by National Key R&D Program of China (grant 2017YFC1500200), the Special Fund of the Institute of Geophysics, China Earthquake Administration (grant DQJB17A01), the National Natural Science Foundation of China (41974100 and 41874074), and the China Scholarship Council.

Appendix A. Supplementary data

Supplementary data to this article can be found online at https://doi.org/10.1016/j.tecto.2021.229104.

References

Ai, S., Zheng, Y., Riaz, M.S., Song, M., Zeng, S., Xie, Z., 2019. Seismic evidence on different rifting mechanisms in southern and northern segments of the Fenhe-Weihe Rift zone. J. Geophys. Res. Solid Earth 124, 609–630. https://doi.org/10.1029/2018JB016476.

An, M., Feng, M., Zhao, Y., 2009. Destruction of lithosphere within the north China craton inferred from surface wave tomography. Geochem. Geophys. Geosyst. 10 (8) https://doi.org/10.1029/2009GC002562. Q08016.

Bao, X., Song, X., Xu, M., Wang, L., Sun, X., Mi, N., et al., 2013. Crust and upper mantle structure of the North China Craton and the NE Tibetan Plateau and its tectonic implications. Earth Planet. Sci. Lett. 369-370, 129–137. https://doi.org/10.1016/j.epsl.2013.03.015.

Bao, X., Song, X., Li, J., 2015. High-resolution lithospheric structure beneath Mainland China from ambient noise and earthquake surface-wave tomography. Earth Planet. Sci. Lett. 417, 132–141. https://doi.org/10.1016/j.epsl.2015.02.024.

Barmin, M.P., Ritzwoller, M.H., Levshin, A.L., 2001. A fast and reliable method for surface wave tomography. Pure Appl. Geophys. 158 (8), 1351–1375. https://doi.org/10.1007/PL00001225.

Bensen, G.D., Ritzwoller, M.H., Barmin, M.P., Levshin, A.L., Lin, F., Moschetti, M.P., et al., 2007. Processing seismic ambient noise data to obtain reliable broad-band surface wave dispersion measurements. Geophys. J. Int. 169 (3), 1239–1260. https://doi.org/10.1111/j.1365-246X.2007.03374.x.

Bodin, T., Sambridge, M., Tkalčić, H., Arroucau, P., Gallagher, K., Rawlinson, N., 2012. Transdimensional inversion of receiver functions and surface wave dispersion. J. Geophys. Res. Solid Earth 117 (2), 1–24. https://doi.org/10.1029/2011JB008560.

Boore, D.M., Nafi Toksöz, M., 1969. Rayleigh wave particle motion and crustal structure. Bull. Seismol. Soc. Am. 59 (1), 331–346.

Chen, W.J., Li, D.M., Dai, T.M., 1992. The K-Ar age and excess Ar of quaternary basalt in Datong. In: Liu, R.X. (Ed.), The Age and Geochemistry of Cenozoic Volcanic Rock in China. Seismology Press, Beijing, pp. 81–92.

Chen, L., Cheng, C., Wei, Z., 2009. Seismic evidence for significant lateral variations in lithospheric thickness beneath the central and western North China Craton. Earth Planet. Sci. Lett. 286 (1–2), 171–183. https://doi.org/10.1016/j.epsl.2009.06.022.

Chen, L., Jiang, M., Yang, J., Wei, Z., Liu, C., Ling, Y., 2014. Presence of an intralithospheric discontinuity in the central and western North China Craton: implications for destruction of the craton. Geology 42 (3), 223–226. https://doi.org/10.1130/G35010.1.

Cheng, C., Chen, L., Yao, H., Jiang, M., Wang, B., 2013. Distinct variations of crustal shear wave velocity structure and radial anisotropy beneath the North China Craton and tectonic implications. Gondwana Res. 23 (1), 25–38. https://doi.org/10.1016/j.gr.2012.02.014.

ChinArray-Himalaya, 2011. China Seismic Array Waveform Data of Himalaya Project. Institute of Geophysics, China Earthquake Administration, Beijing. https://doi.org/10.12001/ChinArray.Data.

Chong, J., Ni, S., Zhao, L., 2015. Joint inversion of crustal structure with the Rayleigh Wave phase velocity dispersion and the ZH Ratio. Pure Appl. Geophys. 172 (10), 2585–2600. https://doi.org/10.1007/s00024-014-0902-z.

Deng, J., Wang, Q., Huang, D., 2005. Basement evolution of the Ordos Basin and its constraint on cap rock. Earth Sci. Front. 12 (3), 91–99.

Dziewonski, A.M., Anderson, D.L., 1981. Preliminary reference Earth model. Phys. Earth Planet. Inter. 25 (4), 297–356. https://doi.org/10.1016/0031-9201(81)90046-7.

Fang, L., Wu, J., Ding, Z., Panza, G.F., 2010. High resolution Rayleigh wave group velocity tomography in North China from ambient seismic noise. Geophys. J. Int. 181 (2), 1171–1182. https://doi.org/10.1111/j.1365-246X.2010.04571.x.

Ferreira, A.M.G., Woodhouse, J.H., 2007. Observations of long period Rayleigh wave ellipticity. Geophys. J. Int. 169 (1), 161–169. https://doi.org/10.1111/j.1365-246X.2006.03276.x.

Griffin, W.L., Andi, Z., O'Reilly, S.Y., Ryan, C.G., 1998. Phanerozoic evolution of the lithosphere beneath the Sino-Korean craton. In: Mantle Dynamics and Plate Interactions in East Asia, pp. 107–126.

Guo, Z., Chen, Y.J., 2017. Mountain building at northeastern boundary of Tibetan Plateau and craton reworking at Ordos block from joint inversion of ambient noise tomography and receiver functions. Earth Planet. Sci. Lett. 463, 232–242. https://doi.org/10.1016/j.epsl.2017.01.026.

Guo, Z., Chen, Y.S., Yin, W.W., 2015. Three-dimensional crustal model of Shanxi graben from 3D joint inversion of ambient noise surface wave and Bouguer gravity anomalies. Chin. J. Geophys. 58 (3), 821–831.

Guo, Z., Chen, Y.J., Ning, J., Yang, Y., Afonso, J.C., Tang, Y., 2016. Seismic evidence of on-going sublithosphere upper mantle convection for intra-plate volcanism in Northeast China. Earth Planet. Sci. Lett. 433, 31–43. https://doi.org/10.1016/j.epsl.2015.09.035.

Haario, H., Laine, M., Mira, A., Saksman, E., 2006. DRAM: efficient adaptive MCMC. Stat. Comput. 16 (4), 339–354. https://doi.org/10.1007/s11222-006-9438-0.

Hauksson, E., Haase, J.S., 1997. Three-dimensional V-P and V-P/V-S velocity models of the Los Angeles basin and central Transverse Ranges, California. J. Geophys. Res. 102 (B3), 5423–5453. https://doi.org/10.1029/96JB03219.

Herrmann, R.B., 1973. Some aspects of band-pass filtering of surface waves. Bull. Seismol. Soc. Am. 663 (2), 663–671.

Hu, S., He, L., Wang, J., 2000. Heat flow in the continental area of China: a new data set. Earth Planet. Sci. Lett. 179 (2), 407–419. https://doi.org/10.1016/S0012-821X(00)00126-6.

Huang, J., Zhao, D., 2004. Crustal heterogeneity and seismotectonics of the region around Beijing, China. Tectonophysics 385 (1–4), 159–180. https://doi.org/10.1016/j.tecto.2004.04.024.

Huang, J., Zhao, D., 2006. High-resolution mantle tomography of China and surrounding regions. J. Geophys. Res. Solid Earth 111 (9), 1–21. https://doi.org/10.1029/2005JB004066.
Huang, Z., Li, H., Zheng, Y., Peng, Y., 2009. The lithosphere of North China Craton from surface wave tomography. Earth Planet. Sci. Lett. 288 (1–2), 164–173. https://doi.org/10.1016/j.epsl.2009.09.019.
Jiang, M., Ai, Y., Chen, L., Yang, Y., 2013. Local modification of the lithosphere beneath the central and western North China Craton: 3-D constraints from Rayleigh wave tomography. Gondwana Res. 24 (3–4), 849–864. https://doi.org/10.1016/j.gr.2012.06.018.
Langston, C.A., 2011. Wave-field continuation and decomposition for passive seismic imaging under deep unconsolidated sediments. Bull. Seismol. Soc. Am. 101 (5), 2176–2190. https://doi.org/10.1785/0120100299.
Laske, G., Masters, G., Ma, Z., Pasyanos, M., 2013. Update on CRUST1.0 – a 1-degree global model of Earth's crust. In: Geophys. Res. Abstr, Vol. 15, p. 2658.
Lei, J., 2012. Upper-mantle tomography and dynamics beneath the North China Craton. J. Geophys. Res. Solid Earth 117 (6), 1–29. https://doi.org/10.1029/2012JB009212.
Levshin, A.L., Ritzwoller, M.H., 2001. Automated detection, extraction, and measurement of regional surface waves. Pure Appl. Geophys. 158 (8), 1531–1545. https://doi.org/10.1007/978-3-0348-8264-4_11.
Levshin, A.L., Barmin, M.P., Ritzwoller, M.H., Trampert, J., 2005. Minor-arc and major-arc global surface wave diffraction tomography. Phys. Earth Planet. Inter. 149 (3–4), 205–223. https://doi.org/10.1016/j.pepi.2004.10.006.
Li, Y., Zhang, J., Guo, L., Zhang, Z., Zhang, J., 2005. Counterclockwise rotation and geodynamics of Ordos block. J. Geod. Geodyn. 25 (3), 50–56.
Li, Y., Wu, Q., Zhang, R., Pan, J., Zhang, F., Zeng, R., 2009. The lithospheric thinning of the North China Craton inferred from Rayleigh waves inversion. Geophys. J. Int. 177 (3), 1334–1342. https://doi.org/10.1111/j.1365-246X.2009.04169.x.
Li, G., Chen, H., Niu, F., Guo, Z., Yang, Y., Xie, J., 2016. Measurement of Rayleigh wave ellipticity and its application to the joint inversion of high-resolution S wave velocity structure beneath Northeast China. J. Geophys. Res. Solid Earth 121 (2), 864–880. https://doi.org/10.1002/2015JB012459.
Li, G., Niu, F., Yang, Y., Xie, J., 2018a. An investigation of time-frequency domain phase-weighted stacking and its application to phase-velocity extraction from ambient noise's empirical Green's functions. Geophys. J. Int. 212 (2), 1143–1156. https://doi.org/10.1093/gji/ggx448.
Li, S., Guo, Z., Chen, Y.J., Yang, Y., Huang, Q., 2018b. Lithospheric structure of the northern Ordos from ambient noise and teleseismic surface wave tomography. J. Geophys. Res. Solid Earth 123 (8), 6940–6957. https://doi.org/10.1029/2017JB015256.
Li, G., Niu, F., Yang, Y., Tao, K., 2019. Joint inversion of Rayleigh Wave phase velocity, particle motion, and teleseismic body wave data for sedimentary structures. Geophys. Res. Lett. 46 (12), 6469–6478. https://doi.org/10.1029/2019GL082746.
Lin, F.C., Schmandt, B., 2014. Upper crustal azimuthal anisotropy across the contiguous U.S. determined by Rayleigh wave ellipticity. Geophys. Res. Lett. 41 (23), 8301–8307. https://doi.org/10.1002/2014GL062362.
Lin, F.C., Ritzwoller, M.H., Snieder, R., 2009. Eikonal tomography: surface wave tomography by phase front tracking across a regional broad-band seismic array. Geophys. J. Int. 177 (3), 1091–1110. https://doi.org/10.1111/j.1365-246X.2009.04105.x.
Lin, F.C., Schmandt, B., Tsai, V.C., 2012. Joint inversion of Rayleigh wave phase velocity and ellipticity using USArray: constraining velocity and density structure in the upper crust. Geophys. Res. Lett. 39 (12) https://doi.org/10.1029/2012GL052196.
Lin, F.C., Tsai, V.C., Schmandt, B., 2014. 3-D crustal structure of the western United States: application of Rayleigh-wave ellipticity extracted from noise cross-correlations. Geophys. J. Int. 198 (2), 656–670. https://doi.org/10.1093/gji/ggu160.
Liu, M., Cui, X., Liu, F., 2004. Cenozoic rifting and volcanism in eastern China: a mantle dynamic link to the Indo-Asian collision? Tectonophysics 393 (1–4 SPEC.ISS), 29–42. https://doi.org/10.1016/j.tecto.2004.07.029.
Liu, C.Y., Zhao, H., Gui, X.J., Yue, L.R., Zhao, J.F., Wang, J.Q., 2006. Space—time coordinate of the evolution and reformation and mineralization response in Ordos Basin. Acta Geol. Sin. 80, 617–638.
Masters, G., Barmine, M., Kientz, S., 2007. Mineos User's Manual in Computational Infrastructure for Geodynamics. Inst. of Technol. Pasadena, Calif.
Menzies, M.A., Fan, W., Ming, Z., 1993. Palaeozoic and Cenozoic lithoprobes and loss of > 120 km of Archaean lithosphere, Sino-Korean craton, China. In: Prichard, H.M., Harris, N.B.W., Neary, C.R. (Eds.), Magmatic Processes and Plate Tectonics, Geol. Soc. Spec. Pub., London, Vol. 76, pp. 71–81.
Menzies, M., Xu, Y., Zhang, H., Fan, W., 2007. Integration of geology, geophysics and geochemistry: a key to understanding the North China Craton. Lithos 96 (1–2), 1–21. https://doi.org/10.1016/j.lithos.2006.09.008.
Mira, A., 2001. On Metropolis-Hasting algorithms with delayed rejection. Metron 59 (3–4), 231–241.
Northrup, C.J., Royden, L.H., Burchfiel, B.C., 1995. Motion of the Pacific plate relative to Eurasia and its potential relation to Cenozoic extension along the eastern margin of Eurasia. Geology 23 (8), 719. https://doi.org/10.1130/0091-7613(1995)023<0719:MOTPPR>2.3.CO;2.
Santosh, M., Zhao, D., Kusky, T., 2010. Mantle dynamics of the Paleoproterozoic North China Craton: a perspective based on seismic tomography. J. Geodyn. 49 (1), 39–53. https://doi.org/10.1016/j.jog.2009.09.043.
Shapiro, N.M., 2005. High-resolution surface-wave tomography from ambient seismic noise. Science 307 (5715), 1615–1618. https://doi.org/10.1126/science.1108339.
Sheehan, A.F., Abers, G.A., Jones, C.H., Lerner-Lam, A.L., 1995. Crustal thickness variations across the Colorado Rocky Mountains from teleseismic receiver functions. J. Geophys. Res. 100 (B10), 20,391–20,404. https://doi.org/10.1029/95JB01966.
Shen, W., Ritzwoller, M.H., Schulte-Pelkum, V., Lin, F.C., 2013. Joint inversion of surface wave dispersion and receiver functions: a Bayesianmonte-Carlo approach. Geophys. J. Int. 192 (2), 807–836. https://doi.org/10.1093/gji/ggs050.
Shen, W., Ritzwoller, M.H., Kang, D., Kim, Y.H., Lin, F.C., Ning, J., et al., 2016. A seismic reference model for the crust and uppermost mantle beneath China from surface wave dispersion. Geophys. J. Int. 206 (2), 954–979. https://doi.org/10.1093/gji/ggw175.
Smith, W.H.F., Wessel, P., 1990. Gridding with continuous curvature splines in tension. Geophysics 55 (3), 293–305. https://doi.org/10.1190/1.1442837.
Tang, Y., Chen, Y., Yang, Y., Ding, Z.-F., Liu, R.-F., Feng, Y.-G., et al., 2011. Ambient noise tomography in North China craton. Chin. J. Geophys. (Acta Geophys. Sin.) 54, 2011–2022. https://doi.org/10.3969/j.issn.0001-5733.2011.08.008.
Tang, Y., Chen, Y.J., Zhou, S., Ning, J., Ding, Z., 2013. Lithosphere structure and thickness beneath the North China craton from joint inversion of ambient noise and surface wave tomography. J. Geophys. Res. Solid Earth 118 (5), 2333–2346. https://doi.org/10.1002/jgrb.50191.
Tanimoto, T., Alvizuri, C., 2006. Inversion of the HZ ratio of microseisms for S-wave velocity in the crust. Geophys. J. Int. 165 (1), 323–335. https://doi.org/10.1111/j.1365-246X.2006.02905.x.
Tanimoto, T., Rivera, L., 2008. The ZH ratio method for long-period seismic data: sensitivity kernels and observational techniques. Geophys. J. Int. 172 (1), 187–198. https://doi.org/10.1111/j.1365-246X.2007.03609.x.
Teng, J.W., Wang, F.Y., Zhao, W.Z., Zhang, Y.Q., Zhang, X.K., Yan, Y.F., Zhao, J.R., Li, M., Yang, H., Zhang, H.S., Ruan, X.M., 2010. Velocity structure of layered block and deep dynamic process in the lithosphere beneath the Yinshan orogenic belt and Ordos Basin. Chin. J. Geophys. Chin. Ed. 53, 67–85. https://doi.org/10.3969/j.issn.0001-5733.2010.01.008.
Tian, Y., Zhao, D., Sun, R., Teng, J., 2009. Seismic imaging of the crust and upper mantle beneath the North China Craton. Phys. Earth Planet. Inter. 172 (3–4), 169–182. https://doi.org/10.1016/j.pepi.2008.09.002.
Vidale, J.E., Helmberger, D.V., 1988. Elastic finite-difference modeling of the 1971 San Fernando, California earthquake (USA). Bull. Seismol. Soc. Am. 78 (1), 122–141.
Waldhauser, F., Lippitsch, R., Kissling, E., Ansorge, J., 2002. High-resolution teleseismic tomography of upper-mantle structure using an a priori three-dimensional crustal model. Geophys. J. Int. 150 (2), 403–414. https://doi.org/10.1046/j.1365-246X.2002.01690.x.
Wang, C.-Y., Sandvol, E., Zhu, L., Lou, H., Yao, Z., Luo, X., 2014a. Lateral variation of crustal structure in the Ordos block and surrounding regions, North China, and its tectonic implications. Earth Planet. Sci. Lett. 387, 198–211. https://doi.org/10.1016/j.epsl.2013.11.033.
Wang, S., Wang, F., Zhang, J., Jia, S., Zhang, C., Zhao, J., Liu, B., 2014b. The P-wave velocity structure of the lithosphere of the North China Craton—results from the Wendeng-Alxa Left Banner deep seismic sounding profile. Sci. China Earth Sci. 57 (9), 2053–2063. https://doi.org/10.1007/s11430-014-4903-7.
Wang, X., Ding, Z., Zhu, L., 2016. Lithospheric Structure of the Northeastern North China Craton Imaged by S Receiver Functions. Pure Appl. Geophys. 173 (8), 2727–2736. https://doi.org/10.1007/s00024-016-1293-0.
Wang, W., Wu, J., Fang, L., Lai, G., Cai, Y., 2017. Sedimentary and crustal thicknesses and Poisson's ratios for the NE Tibetan Plateau and its adjacent regions based on dense seismic arrays. Earth Planet. Sci. Lett. 462, 76–85. https://doi.org/10.1016/j.epsl.2016.12.040.
Xu, P., Zhao, D., 2009. Upper-mantle velocity structure beneath the North China Craton: implications for lithospheric thinning. Geophys. J. Int. 177 (3), 1279–1283. https://doi.org/10.1111/j.1365-246X.2009.04120.x.
Xu, Y., Chung, S., Ma, J., Shi, L., 2004. Contrasting cenozoic lithospheric evolution and architecture in the Western and Eastern Sino-Korean Craton: constraints from geochemistry of basalts and mantle xenoliths. J. Geol. 112 (5), 593–605. https://doi.org/10.1086/422668.
Xu, Y.G., Ma, J.L., Frey, F.A., Feigenson, M.D., Liu, J.F., 2005. Role of lithosphere-asthenosphere interaction in the genesis of Quaternary alkali and tholeiitic basalts from Datong, western North China Craton. Chem. Geol. 224 (4), 247–271. https://doi.org/10.1016/j.chemgeo.2005.08.004.
Xu, H., Luo, Y., Yang, Y., Shen, W., Yin, X., Chen, G., et al., 2020. Three-dimensional crustal structures of the Shanxi Rift constructed by Rayleigh wave dispersion curves and ellipticity: implication for sedimentation, intraplate volcanism, and seismicity. J. Geophys. Res. Solid Earth 125. https://doi.org/10.1029/2020JB020146 e2020JB020146.
Yang, Y., Ritzwoller, M.H., Levshin, A.L., Shapiro, N.M., 2007. Ambient noise Rayleigh wave tomography across Europe. Geophys. J. Int. 168 (1), 259–274. https://doi.org/10.1111/j.1365-246X.2006.03203.x.
Yano, T., Tanimoto, T., Rivera, L., 2009. The ZH ratio method for long-period seismic data: Inversion for S-wave velocity structure. Geophys. J. Int. 179 (1), 413–424. https://doi.org/10.1111/j.1365-246X.2009.04293.x.
Yao, H., Beghein, C., Van Der Hilst, R.D., 2008. Surface wave array tomography in SE Tibet from ambient seismic noise and two-station analysis – II. Crustal and upper-mantle structure. Geophys. J. Int. 173 (1), 205–219. https://doi.org/10.1111/j.1365-246X.2007.03696.x.
Yin, A., Harrison, T.M., 2000. E Volution of the H Ealth C are. Annu. Rev. Earth Planet. Sci. 28, 211–280. https://doi.org/10.1080/01947641003598252.
Zhang, Y.Q., Mercier, J.L., Vergély, P., 1998. Extension in the graben systems around the Ordos (China), and its contribution to the extrusion tectonics of South China with respect to Gobi-Mongolia. Tectonophysics 285 (1–2), 41–75. https://doi.org/10.1016/S0040-1951(97)00170-4.
Zhang, Y., Ma, Y., Yang, N., Shi, W., Dong, S., 2003. Cenozoic extensional stress evolution in North China. J. Geodyn. 36 (5), 591–613. https://doi.org/10.1016/j.jog.2003.08.001.

Zhao, D., Kanamori, H., Negishi, H., Wiens, D., 1996. Tomography of the source area of the 1995 Kobe earthquake: evidence for fluids at the hypocenter? Science 274 (5294), 1891–1894. https://doi.org/10.1126/science.274.5294.1891.

Zhao, G., Sun, M., Wilde, S.A., Sanzhong, L., 2005. Late Archean to Paleoproterozoic evolution of the North China Craton: key issues revisited. Precambrian Res. 136 (2), 177–202. https://doi.org/10.1016/j.precamres.2004.10.002.

Zhao, L., Allen, R.M., Zheng, T., Hung, S.H., 2009. Reactivation of an Archean Craton: constraints from P- and s-wave tomography in North China. Geophys. Res. Lett. 36 (17), 1–5. https://doi.org/10.1029/2009GL039781.

Zhao, L., Allen, R.M., Zheng, T., Zhu, R., 2012. High-resolution body wave tomography models of the upper mantle beneath eastern China and the adjacent areas. Geochem. Geophys. Geosyst. 13 (6), 1–20. https://doi.org/10.1029/2012GC004119.

Zhang, S., 2000. Basin evolutionary differences and seismotectonics of Fenwei Graben system (in Chinese with English abstract). Journal of Geomechanics 6 (2), 30–37. https://doi.org/10.3969/j.issn.1006-6616.2000.02.006.

Zheng, S., Sun, X., Song, X., Yang, Y., Ritzwoller, M.H., 2008. Surface wave tomography of China from ambient seismic noise correlation. Geochem. Geophys. Geosyst. 9 (5), 1–8. https://doi.org/10.1029/2008GC001981.

Zheng, T., Zhao, L., Zhu, R., 2009. New evidence from seismic imaging for subduction during assembly of the North China craton. Geology 37 (5), 395–398. https://doi.org/10.1130/G25600A.1.

Zheng, Y., Shen, W., Zhou, L., Yang, Y., Xie, Z., Ritzwoller, M.H., 2011. Crust and uppermost mantle beneath the North China Craton, northeastern China, and the Sea of Japan from ambient noise tomography. J. Geophys. Res. 116 (B12), B12312 https://doi.org/10.1029/2011JB008637.

Zhu, R., Chen, L., Wu, F., Liu, J., 2011. Timing, scale and mechanism of the destruction of the North China Craton. Sci. China Earth Sci. 54 (6), 789–797. https://doi.org/10.1007/s11430-011-4203-4.

Zhu, R., Xu, Y., Zhu, G., Zhang, H., Xia, Q., Zheng, T., 2012. Destruction of the North China Craton. Sci. China Earth Sci. 55 (10), 1565–1587. https://doi.org/10.1007/s11430-012-4516-y.